ACS Photonics

pubs.acs.org/journal/apchd5 Article

High Interharmonic Generation from Isolated Bound States

Sergey Hazanov,[#] Alexey Gorlach,[#] Ron Ruimy, Dmitry Yakushevskiy, Matan Even Tzur, Marcelo F. Ciappina, and Ido Kaminer*

Cite This: https://doi.org/10.1021/acsphotonics.4c02095 Read Online

ACCESS | Metrics & More | Article Recommendations | Supporting Information

ABSTRACT: High harmonic generation (HHG) is a nonlinear process in which systems driven by an intense laser emit integer harmonics of the driving field. Here we report that the strong nonlinear response of systems with isolated bound states split the HHG spectrum into nonharmonic Mollow-type triplets that reveal the internal electronic dynamics. We identify the conditions required to observe these phenomena and propose potential experimental systems that could enable their detection. Our findings offer new insights into the fundamental physics of HHG and may have applications in high-harmonic spectroscopy, X-ray physics, and the study of ultrafast dynamics.

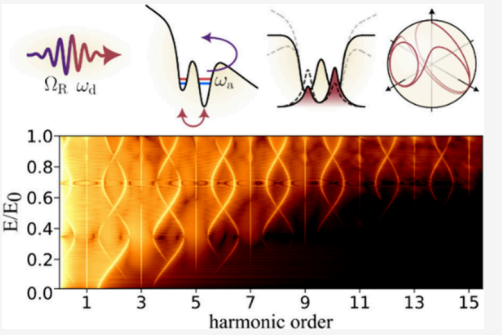

KEYWORDS: *high harmonic generation, extreme nonlinear optics, Mollow-triplets, attosecond physics, hyper Raman lines*

INTRODUCTION

When driven by an intense laser pulse, different types of systems, such as atoms, molecules, and more recently solids, can emit photons at frequencies that are integer multiples of the driving field. This highly nonlinear effect is known as high harmonic generation (HHG).[1−3] The electron dynamics during HHG is usually well-described by the three-step model:[2] An electron escapes the potential barrier of the atom, accelerates by the driving field, and recombines with the nucleus to emit harmonics. These main features of HHG, such as its spectrum, are universal and appear in a wide range of systems. These features were described over the years by many theories, for example, as self-modulation of light traversing a medium due to its Kerr response time.[4−6]

HHG spectrum has characteristic features: its frequency range extends beyond the ionization potential of the atom with uniform intensity (the so-called plateau), which then abruptly falls off (the cutoff). The HHG spectrum has only odd harmonics of the driving frequency ω_d due to the inversion symmetry of the atom,[7]

$$\omega_{\mathrm{HHG}}^{(n)} = (2n+1)\omega_d, \quad n \in \{1, 2, \ldots\} \tag{1}$$

Under certain circumstances, the spectrum of the emitted radiation can deviate from this simple formula. First, symmetry breaking leading to even harmonics generation was shown both in theory,[7−11] and experimentally,[12,13] More intricate scenarios can occur when the external field is manipulated by changing the carrier-envelope phase, resulting in a global spectral shift,[14] employing two drive tones in order to induce transitions resulting in hyper-Raman lines,[15,16] or in the presence of beating between frequency of charge motion and driving field.[17]

In this work, we consider the dynamics of an electron inside its potential as a source for high interharmonic generation (HIG): Tuning the external field to interact with an isolated electronic transition of the given system results in Rabi floppings which in turn imprint the modulation of the polarization on the spectrum emitted by the driven system.[18] In the limit of a weak external field, the polarization is modulated sinusoidally, resulting in the famous Mollow triplet.[19] Upon reaching the regime where the external field is comparable in strength with the addressed electronic transition, the polarization of the corresponding transition is modulated in a more complicated way, resulting in carrier-wave Rabi floppings.[20] These give rise to carrier-wave Mollow triplets, or Mollow triplets around higher order (odd) harmonics. This phenomenon was studied theoretically in the context of two-level systems (TLSs)[21−24] and in 1D systems involving double-well potentials.[25−28] While these works covered much of the underlying physics, they provided little evidence for experimental feasibility, focusing on ideal TLSs and infinite potential wells. An exception is,[27] where HHG from hydrogen molecular ions, H_2^+, was shown by simulation to contain HIG, albeit in a limited configuration of

Received: October 25, 2024
Revised: December 28, 2024
Accepted: December 30, 2024

parameters and missing the broader context of the phenomenon. In a related work,[28] the authors demonstrate evidence for carrier-wave Rabi floppings in alkali atoms, considering realistic experimental settings. These works highlight that traditional HHG settings cannot give rise to the full scale of HIG and its related effects due to carrier-wave Rabi floppings, as will be shown in this work.

Experimental efforts to reach this regime of extreme nonlinear optics focused on semiconductors,[29,30] and more recently in the microwave regime with NV centers.[31,32] However, to the best of our knowledge, this phenomenon was not observed experimentally in the optical regime.

Here we study the dynamics of multilevel systems beyond the rotating-wave approximation, considering ionization and continuum. We discover a mechanism generating interharmonic features in the HHG spectra of atomic systems, rooted in the motion of the electron's wave packet within its potential well, manifesting the carrier-wave Rabi floppings between isolated bound states. Our proof-of-concept simulations demonstrate these features in several one-dimensional potentials with fixed nuclei, adhering to common HHG simulation methods.

We demonstrate that these features, adjustable by the driver intensity and frequency, imprint the potential's shape and energy-level structures onto both the HHG spectrum and the temporal shape of the emitted radiation. In addition, we demonstrate that this phenomenon is related to the localization of the electron's wave packet and identify the universal nature of this effect by demonstrating it in a range of different potentials. These universal interharmonic features connect a simpler TLS model with practical instances in solid-HHG,[12,33−35] THz pulse-driven HHG,[36] HHG from ionized atoms and molecules, and analogous effects in spin systems.[31,32] Our findings provide the recipe for future experiments that could observe HIG in these systems. These singular HHG regimes can lead to applications in attoscience, X-ray physics, and coherent control of core electrons, unveiling new processes in strongly driven systems and providing a better understanding of existing ones.

Dressing the Spectrum of HHG. To motivate the study of HHG from potentials with isolated bound states, we begin by revisiting the nonlinear response of a TLS in an intense external drive. Consider a TLS of energy separation $\hbar\omega_a$, a driving field with frequency ω_d, and a constant amplitude, corresponding to a Rabi frequency Ω_R (see eq S1). In the case of a resonant drive with $\Omega_R \lesssim \omega_a$, the system is excited by absorption and de-excited via stimulated emission, leading to sinusoidal modulation of the polarization, proportional to cos $\Omega_R t$. In this regime, we identify a single dominant Mollow triplet,[18,19,37] whose central spectral line $\omega = \omega_d = \omega_a$ is dressed by two sidebands at frequencies $\omega = \omega_a \pm \Omega_R$, corresponding to the Fourier transform of the polarization.

In the extreme nonlinear regime, where $\Omega_R \gtrsim \omega_a$, the polarization no longer follows a simple sinusoidal modulation. The resulting modulation is known as carrier-wave Rabi floppings[20] and the corresponding emission spectrum admits additional spectral triplets, which are known as carrier-wave Mollow triplets.[18,38] The central lines of these triplets coincide with the odd harmonics of the driving frequency, and the two sidebands pertain to interharmonic generation, with frequencies approximated by[27,39] (appearing as Floquet quasienergies of the driven system):

$$\omega^{(n)}_{\mathrm{HIG},\pm} = (2n+1)\omega_d \mp \left[\omega_d - \omega_a \cdot J_0\left(2\Omega_R/\omega_d\right)\right] \tag{2}$$

where $n \in \{1, 2, ...\}$ and J_0 is the zeroth-order Bessel function of the first kind. The regime in which the last term of eq 2 approaches zero has been studied in the context of tunneling cancelation and localization,[37,40] and referred to as the degeneracy points of the Floquet quasienergies (see the Supporting Information for the corresponding simulations in TLSs).

Our work demonstrates how Mollow-like triplets can be imprinted on the HHG spectrum by considering potentials with isolated bound states (i.e., energy separation significantly smaller than the ionization threshold). This setup closely resembles ideal TLSs, which strongly differ from the more conventional situations of Hydrogen-like potentials. In contrast, double-well potentials are suitable candidates since they serve as a textbook system for controlling degeneracy and its splitting that creates two neighboring energy levels. Figure 1a schematically depicts how this can be achieved: We drive an atomic system containing isolated bound states by a properly

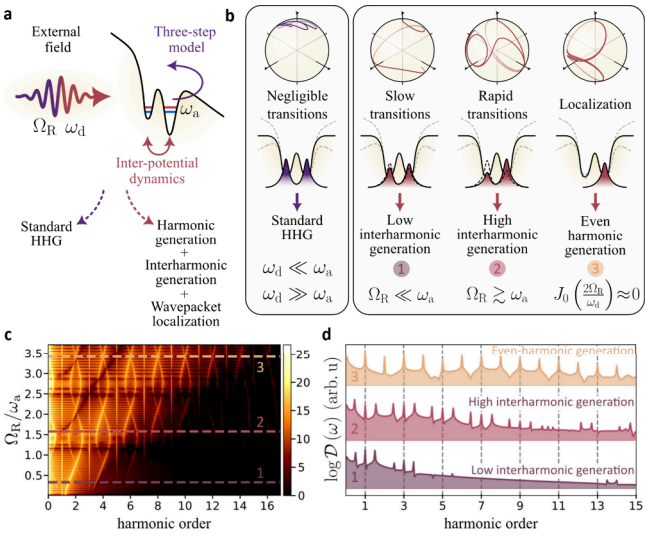

Figure 1. Imprinting the dynamics of bound states on the spectrum of high harmonic generation (HHG). (a) Schematic representation of harmonic generation from isolated bound states. (b) Correspondence between the dynamics of the isolated bound states, represented with the pertaining Bloch spheres, and the motion of the wavepacket within the potential. The dynamics can be divided into standard HHG-like dynamics, with negligible dynamics in the TLS subspace (left column), and the regime of efficient interharmonic generation (right group of columns). The curve on each Bloch sphere represents the direction of the Bloch vector while the external field is on. (c) Emission spectra of an electron in a double-well potential subjected to an external field with $\omega_d = 0.8\omega_a$ ($\hbar\omega_a$ being the energy separation of the two lowest bound states of the stationary potential) and different field amplitudes (vertical axis). For each amplitude (corresponding to a different Rabi frequency, see Methods), we solve the Schrödinger equation and compute the emission spectrum. The color encoding represents the dipole spectrum on a logarithmic scale, log $\mathcal{D}(\omega)$ (see Methods). The parameters for these simulations (external field, stationary potential, and grids parameters) are summarized in Tables S1−S3 (Supporting Information). The relation between the field amplitude and the Rabi frequency is found by fitting the interharmonic spectral lines with those of an ideal TLS (Supporting Information). (d) Three emission spectra correspond to lines 1, 2, and 3 in (b) and (c).

https://doi.org/10.1021/acsphotonics.4c02095
ACS Photonics XXXX, XXX, XXX−XXX

chosen intense laser field. The resulting dynamics resemble that of the well-known three-step model, overlaid by intrapotential dynamics within the isolated bound states, leading to a radiation spectrum that mixes both traditional HHG and HIG.

When considering atomic systems with isolated bound states, we can observe four distinct regimes (see Figure 1b):

- First, an off-resonance external drive frequency, far from the isolated states, e.g., $\omega_d \ll \omega_a$, leads to negligible intrapotential dynamics and does not contribute to the emitted spectrum (left sketch in Figure 1b). In the Bloch sphere representation, this regime corresponds to the Bloch vector remaining near the ground state pole.
- Second, an external drive corresponding to $\Omega_R \ll \omega_a$, close in frequency to the isolated states transition, $\omega_d \sim \omega_a$, leads to slow, almost-sinusoidal dynamics between the isolated bound states and results in low-order interharmonic generation (second from the left sketch in Figure 1b). In the Bloch sphere representation, this regime corresponds to the Bloch vector's motion spreading across the sphere.
- Third, an external drive with an increased amplitude that reaches the regime, where $\Omega_R \gtrsim \omega_a$, leads to high interharmonic generation and rapid, nonsinusoidal Rabi oscillations (third from the left sketch in Figure 1b). In the Bloch sphere representation, this regime corresponds to the Bloch vector tracing a trajectory similar to that of carrier-wave Rabi floppings.
- Fourth, taking Ω_R to satisfy the condition $J_0(2\Omega_R/\omega_d) = 0$ (see eq 1), and then the dynamics between two isolated states adheres to an equal superposition, leading to the localization of the electron's wavepacket and resulting in the emission of even-harmonics (right sketch in Figure 1b). In terms of the Bloch sphere, this regime corresponds to the Bloch vector remaining around the equator for an extended duration.

Another distinct scenario (not depicted) appears inside the second regime above, when the external field is weak, $\Omega_R \ll \omega_a$, but on resonance with the transition, $\omega_d = \omega_a$. In this case, conventional Rabi-floppings contribute to the emission of a single Mollow-triplet. Figure 1c,d shows an example of the external field amplitude-dependent emission spectrum of an electron in a double-well potential. For each amplitude, the emission spectrum is computed by numerically solving a 1D time-dependent Schrödinger equation and employing the single-active-electron (SAE) approximation. The HIG shows as braids around the odd-harmonic spectral lines (traditional HHG), following eq 2. In Figure 1d, three cross sections are presented, showing the limit of a weak driving field (zero-order Mollow triplet), an example of a strong drive (many orders of triplets) and even-harmonic generation occurring at the intersection of adjacent sidebands.

HIG, as described by eq 2, is most efficient when the external driving field can generate TLS-like dynamics in isolated bound states. Figure 2 compares the emission spectra of single-, double-, and triple-well potentials under a nonresonant ($\omega_a \neq \omega_d$) intense external field. Here we demonstrate that HIG arising from TLS-like dynamics constraints not only the values of ω_a,ω_d and Ω_R, but also requires the presence of *isolated* bound states. In Figure 2a, an electron bounded by a single-well Coulomb potential and driven by a laser with $\omega_d = 1.55$ eV emits only odd harmonics

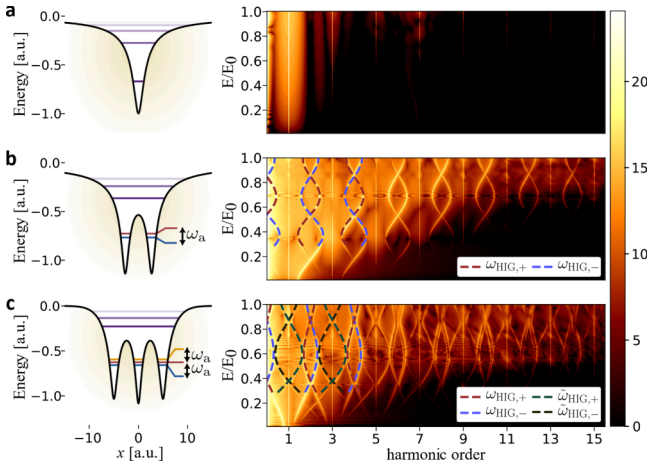

Figure 2. Isolated bound states as a source for efficient interharmonic generation (HIG). The color map indicates the dipole spectrum on a logarithmic scale, log $\mathcal{D}(\omega)$ (see Methods). The reference amplitude $E_0 = 0.0534$ au corresponds to an intensity of $I = 1 \times 10^{14}$ W cm^{-2}. (a) Single-well (Coulomb) potential (left) and the corresponding traditional HHG spectrum, having only odd harmonics. (b) Double-well potential: the HHG spectrum of odd harmonics is supplemented by the interharmonic lines described by eq 2. (c) Triple-well potential: the spectrum has additional spectral lines described by eqs 2−3). The external pulse of the trapezoidal shape is characterized by $(n_{on},n_p,n_{off}) = (1,50,1)$ (see Methods). In (a), the carrier frequency is $\omega_d = 0.057$ au(1.55 eV) with $\Delta\varepsilon_{10} = 0.395$ au(10.75 eV) and in (b) and (c), the carrier frequency is $\omega_d = 0.7\omega_a$, with $\omega_a = 0.04$ au (1.09 eV) in (b) and $\omega_a = 0.032$ au (0.87 eV) in (c) (the rest of the simulation parameters can be found in Tables S1−S3 in the Supporting Information).

of ω_d. On the contrary, for an electron in the double- and triple-well potentials driven by a field with $\omega_d = 0.7\omega_a$ we observe strong HIG (see Figure 2b,c). In the extreme nonlinear regime, the interharmonic spectral lines are well described by eq 2. As mentioned above, the external field does not have to be resonant with any transition for HIG to occur.

More complicated well-type structures give rise to more intricate interharmonic spectra. We consider a triple-well potential such that the three lowest eigenenergies are equidistant, $\Delta\varepsilon_{10} \approx \Delta\varepsilon_{21} \equiv \hbar\omega_a$. Driving this system by a field with $\omega_d = 0.7\omega_a$ results in the emission spectrum depicted in Figure 2c. This spectrum exhibits contributions from three individual TLSs: ground and first excited state, first excited state and second excited state, and the ground and second excited state having energy separation $2\omega_a$. The blue and red dashed lines in Figure 2c correspond to eq 2 evaluated for $\hbar\omega_a = \Delta\varepsilon_{10} \approx \Delta\varepsilon_{21}$. Interestingly, the spectral lines of the TLS with frequency $2\omega_a$ intersect the odd harmonics and cannot be fitted by eq 2. These spectral lines are found to satisfy a modified version of eq 2:

$$\tilde{\omega}^{(n)}_{HIG,\pm} = (2n+1)\omega_d \pm \omega_a^{(3)} J_0\left(2\Omega_R/\omega_d\right) \tag{3}$$

where $\omega_a^{(3)} \approx 2\omega_a$ and $n \in \{0, 1, 3, ...\}$.

The contributions arising from the two equidistant energy levels are predicted by eq 2 to be degenerate. Instead, Figure 2c shows that the degeneracy is lifted by a small "repulsion" between the energy levels, exhibiting a sort of avoided crossing as in many physical systems.[41] This analysis directly generalizes beyond single-, double-, and triple-wells to arbitrary systems. Thus, the shape of the energy potential and its isolated bound

https://doi.org/10.1021/acsphotonics.4c02095
ACS Photonics XXXX, XXX, XXX−XXX

states are imprinted on the HHG spectrum. This mechanism can be exploited for a new type of spectroscopy, where the shape of the interharmonic generation can be resolved to the contributing isolated bound states to reconstruct electronic orbitals of molecules.[42]

Experimental Feasibility. We now consider the feasibility of experimentally reaching the regime of efficient HIG from isolated bound states. First, we consider the effect of the Gaussian envelope of the external field (see Figure 3a,b). This

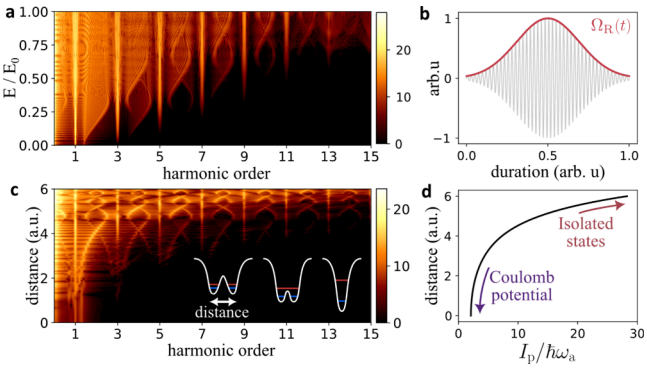

Figure 3. Experimental feasibility. (a) Electron in a double-well potential driven by a Gaussian pulse with t_{fwhm} = 20 optical cycles (shown in the inset). The helix-shaped interharmonic peaks are smeared but can still be resolved. (b) Time profile of the driving field amplitude. The red line (the envelope of the external field) is the time-dependent Rabi frequency, $\Omega_R(t)$. (c) Emission spectra for different double-well potentials with different distances between the wells (vertical axis). The inset shows the typical behavior of the two lowest laying bound states in a double well potential as the distance is varied. The driving field has a constant envelope, and its amplitude is $E = E_0$ for all the simulations and the drive frequency is taken to be $\omega_d = 0.8\omega_a$ (see Tables S1−S3 in the Supporting Information for the rest of the parameters of the simulations). (d) The isolation of the two lowest bound states, $I_p/\hbar\omega_a$, as a function of the distance between the wells. The colormap and the reference amplitude, E_0, are the same as in Figure 2 (for both (a) and (c)).

amounts to a time-dependent Rabi frequency for the Rabi oscillations between the isolated bound states (Figure 3b). As can be seen in Figure 2a, the time-dependent Rabi frequency smears the interharmonic spectral lines predicted by eq 2. Nevertheless, for a sufficiently long pulse (t_{fwhm} = 20 optical cycles in Figure 2a,b), the HIG can still be resolved.

Next, we quantify the isolation of a pair of bound states by considering the ratio between the ionization energy and the energy separation of the two states, $I_p/\hbar\omega_a$, where the ionization is defined as the absolute value of the lowest energy level, $I_p = -E_0$. We then construct double-well potentials with varying distances between the wells and compute the corresponding emission spectrum (Figure 3c,d). The distance is swept between 0, corresponding to a Coulomb-like potential (right sketch in the inset of Figure 3c), and 6, corresponding to a pair of very isolated bound states (left sketch in the inset). For each distance, the energy separation, ω_a, is different, and therefore, the drive frequency is also changed to be $\omega_d = 0.8\omega_a$. Figure 3d shows the ratio $I_p/\hbar\omega_a$ as a function of the distance. This allows us to estimate the parameters that would be required of a real system with a continuum to exhibit HIG from its isolated bound states. From Figure 3c,d we roughly estimate that at distances larger than 3 au or equivalently the ratio $I_p/\hbar\omega_a$ larger than 4, the HIG starts to be visible.

Finally, we discuss realistic systems where HIG from TLS-like dynamics can be observed experimentally. In this work, we focused on the regime where an atomic system mimics the conditions of ideal two-level systems in the form of isolated bound states. However, other types of systems can recreate these conditions as well. For example, interband transitions in semiconductor quantum wells, or spin-systems where two spin states can be brought close together with a magnetic field. Indeed, experiments involving these platforms showed signatures of carrier-wave Rabi floppings and the associated HIG, with GaAs in the THz or Infrared regimes,[29,30,43] and NV-centers in the MW regime.[31,32] Moreover, HHG from semiconductors is now routinely observed in experiments.[12,33,44]

Here we argue that under the conditions that we specified in this section, atomic systems with ionization threshold can support this type of HIG. In,[28] the authors demonstrate, by simulation, that under experimentally feasible conditions, K atoms can emit a spectrum reminiscent of a carrier-wave Mollow triplet (around the third harmonic). This result is consistent with Figure 4(c), where the isolation of $I_p/\hbar\omega \sim 2.7$ (as in the case of Potassium), corresponds to first signs of HIG around the third harmonic. Possible more suitable candidates for efficient HIG are molecules, e.g., molecular iodine, having first ionization energy of I_p = 9.307 eV and an electronic ground ($X0_g^+$) to excited ($B0_u^+$) state transition with $\hbar\omega_a \approx$ 2.294 eV, which corresponds to $I_p/\hbar\omega_a \sim 4.1$.[45,46] Another possibility is H_2^+, which in the large internuclear admits two isolated bound states transition, $1\sigma_g \rightarrow 1\sigma_u$, reaching even larger $I_p/\hbar\omega_a$ ratios.[27] One may also consider HIG from superconducting artificial atoms, where the potential landscape can be engineered to admit very isolated bound states, e.g., the flux qubit[47] that has a double-well energy potential. Zero-order Mollow triplets have already been observed in such systems[48] and ionization in such systems is a research topic of growing interest.[49,50]

Time-Domain Analysis: Intrapotential Dynamics, Localization, and Attosecond Pulse Trains. In this section, we demonstrate the manifestation of carrier-wave Rabi floppings and their generalization to nonresonant drives and multilevel transitions in the evolution of the electron's wavepacket. We also link Floquet quasienergy degeneracy points to instances of localized wavepacket evolution and showcase the effect on the emission of attosecond pulse trains.

Figure 4a1 illustrates electron wavepacket evolution in a Coulomb potential with the driving field initiating HHG but not causing any major dynamics in the two lowest-laying bound states, as can be seen by the projection of their dynamics on the Bloch sphere (Figure 4a2 and Figure 1b). Increasing the field's amplitude results in a rapid depletion of the atom before significant HIG (Figure 4b1,b2). Note that in 1D simulations of HHG, the part of the wavepacket that goes to the continuum (in each cycle of the driving field) is always very small compared to the part that remains bounded. To observe the portion of the wavepacket that ionizes and reaches the boundaries, one has to consider the log magnitude of probability density (see Supporting Information). In Figure 4c1, we show the wavepacket evolution in the typical scenario considered in this work, a double-well potential and off-resonant drive. Extended nondepleting dynamics leads to suboptical-cycle well transitions, resulting in HIG emission and translating to substantial dynamics on the Bloch sphere (Figure 4c2). In Figure 4d we consider the dynamics of an electron in a

https://doi.org/10.1021/acsphotonics.4c02095
ACS Photonics XXXX, XXX, XXX−XXX

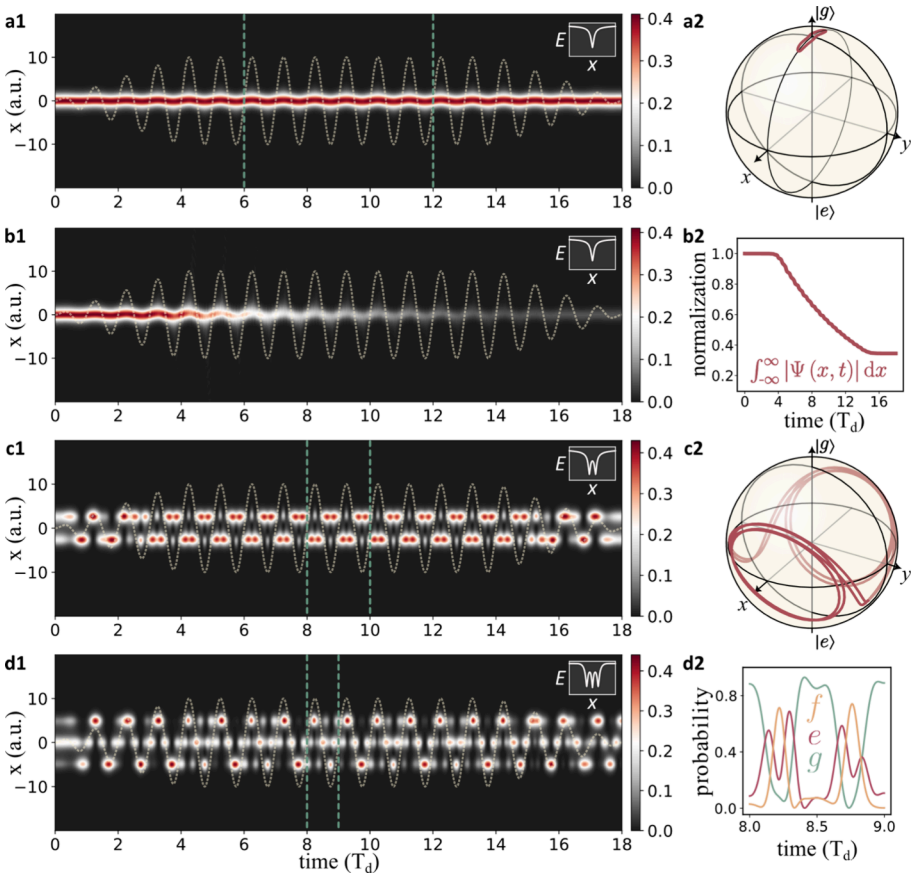

Figure 4. Time-domain analysis: Intrapotential wavepacket dynamics. The color map indicates the magnitude of the electron's probability density, $|\Psi(x,t)|^2$, as a function of x (vertical axis) and t (horizontal axis) in periods of the driving field, $T_d = 2\pi/\omega_d$. Green dashed lines correspond to the period in which the data for the right insets were taken. Yellow dashed lines represent the driving field with the envelope $(n_{on},n_p,n_{off}) = (4,10,4)$ (see Methods). (a1) Electron in the Coulomb potential (same as Figure 2a) with field amplitude $E = E_0$ (E_0 same Figures 2 and 3). (a2) Bloch sphere dynamics corresponding to the two lowest laying bound states (see Supporting Information). (b1) Electron in the Coulomb potential with $E = 1.8E_0$. Most of the wavepacket is absorbed in the boundaries (at $x = \pm 25$ au, not shown for visibility), and the corresponding wavepacket normalization is shown in (b2). (c1) Electron in a double-well potential (same as Figure 2b) performs rapid oscillations without depletion. These oscillations reproduce Bloch vector dynamics akin to that of carrier-wave Rabi floppings, as shown in (c2). (d1) Electron in a triple-well potential (same as Figure 2c). The electron performs rapid oscillations between the three wells, which corresponds to dynamics between the three lowest bound states. (d2) Occupation probability for the three lowest bound states g, e, and f during the period marked between the green dashed lines in (d1).

triple-well potential well (same as in Figure 2c). Here there are even more intricate dynamics, with the electron's wavepacket hopping between the three wells. This complex motion leads to the contributions described in eq 3 on top of those from eq 2, and results in significant dynamics in the first three lowest bound states, g, e, and f (see Figure 4d2).

The intrapotential dynamics, pertaining to floppings between the isolated bound states of the atomic potential, modify the typical trajectories taken by an electron driven in and out of a Coulomb-like potential within the three-step semiclassical picture. Therefore, on top of HIG, we expect modifications to the typical structure of the emitted radiation, such as the cutoff energy, $I_p + 3.17U_p$. Nevertheless, the part of the electron's dynamics resulting in standard HHG takes place in free-space and is not expected to be influenced by the intrapotential dynamics. Thus, we conjecture that modifications to the overall spectral shape of the emitted spectrum will be limited.

The relation between the degeneracy points of the Floquet quasienergies (eq 2) and the cancellation of tunneling between the potential wells was studied both in the context of TLSs[39,51] and double-well potentials.[25,40] In Figure 5, we demonstrate this effect by considering the expectation value of the electron's position, averaged over the entire drive duration, $\mathrm{avg}_{t\in(0,T)} \langle\Psi| x|\Psi\rangle$. Figure 5a shows that as the Rabi frequency (vertical axis), Ω_R, is swept across a zero of the Bessel function in eq 2 (Floquet quasienergy degeneracy), the emission spectrum turns purely harmonic (including even harmonics) and the electron's wavepacket quickly alternates between localizing in the left and right wells. In Figure 5b,c, the electron spends the majority of the drive duration in the left (right) well, corresponding to a negative (positive) average position (averaged over the entire duration of the driving field) and to the minimum (maximum) of the green curve in Figure 5a. This description is consistent with 25, where the localization was found to occur for parameter sets (Ω_R,ω_d) in the proximity of the zeros of the Bessel function, rather than at the exact zeros. Our description shows for the first time, to the best of our knowledge, the behavior of localization around the degeneracy points Figure. 5d, shows the Bloch vector dynamics of the isolated bound states during localization in the right well (during the period marked by the green dashed line in Figure

https://doi.org/10.1021/acsphotonics.4c02095
ACS Photonics XXXX, XXX, XXX−XXX

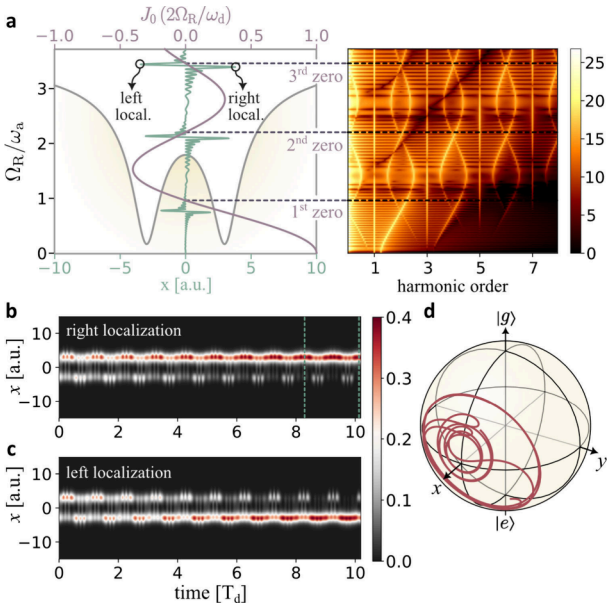

Figure 5. Time-domain analysis: Wavepacket localization and Floquet quasienergies degeneracy. (a) Same system as in Figure 1c. The green line and the bottom x-axis correspond to the expectation value of the electron's position, averaged over the entire duration of the driving field, $\text{avg}_{t\in(0,T)}\langle\Psi(x,t)|x|\Psi(x,t)\rangle$ (the value is multiplied by three to make it more visible w.r.t. the stationary potential). The purple line and the top x-axis correspond to the Bessel function appearing in the Floquet quasienergies of eq 2. Its zeros are matched with the actual energy degeneracies appearing in the emission spectra heatmap on the right. The energy units of the stationary potential are omitted for visibility. (b, c) Right and left wavepacket localizations (seen as peaks in the green line in (a)) occur in the vicinity of degeneracies in the quasienergies (marked with purple dashed lines) and the zeros of the Bessel function in eq 2. (d) Bloch vector evolution in time (dashed green lines in (b)). The $|g\rangle$ (top) and $|e\rangle$ (bottom) states of the Bloch sphere are defined as the two lowest eigenstates of the double-well potential.

5b). During this duration, the Bloch vector points mostly in the x direction (see Supporting Information for the TLS analogy). We note that a similar localization mechanism was proposed in solid-state HHG.[52]

Finally, we find that the presence of isolated bound states is imprinted on the emitted attosecond pulse trains (see the Supporting Information for attosecond pulse train reconstruction). We compare a single-well (Coulomb) and a double-well potential, both having the same ionization energy and driven by the same external field. The emitted attosecond pulses are depicted in Figure 6a,b and appear to be distinct. Figure 6c shows the emission spectrum in both cases, showing only odd harmonics for the single-well case, and odd harmonics with HIG for the double-well potential. The distinct features of the emitted attosecond pulses can be exploited to algorithmically unveil the exact shape of the potential, characteristics of the driving field and the dynamics of the electron, providing an innovative type of inverse scattering in a highly nonlinear system. For example, to observe localization of the electron. This approach opens new possibilities for spectroscopy and attosecond pulse shaping.

CONCLUSIONS

We conclude that efficient HIG from bound states dynamics requires the states to be isolated from the ionization threshold

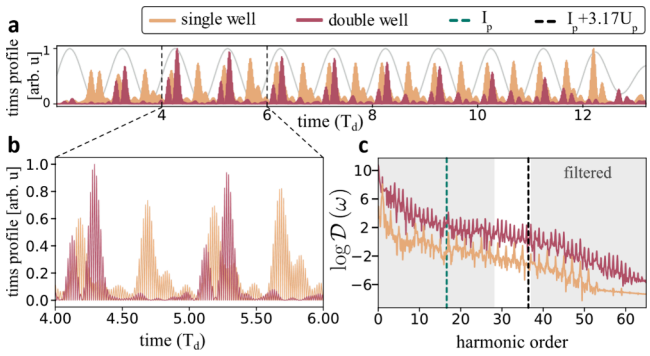

Figure 6. Emitted attosecond pulse trains in the presence of isolated bound states. (a) Trains of attosecond pulses for the single-well (yellow) and double-well (red) potentials. The shapes of the potentials are chosen such that both have the same ionization energy I_p (see Supporting Information for the simulation parameters). The time axis is in units of the driving field period, $T_d = 2\pi/\omega_d$. (b) Zoom in on the emitted pulse train between four and five periods of the external field. (c) To extract the attosecond pulses, we filtered the dipole acceleration (see eq 9 in the Methods), comparing the contribution from the harmonics 28 to 37 in both cases, indicated by the gray boundary in the panel. The green dashed line corresponds to the ionization energy and the black dashed line to the usual cutoff frequency in HHG experiments, $I_p + 3.17U_p$, where U_p is the pondermotive energy.

quantified by the ionization-to-energy-separation ratio $I_p/\hbar\omega_a$. We demonstrated that the emission of amplitude-dependent interharmonic peaks, previously attributed mainly to TLSs, can be exhibited by atomic systems under appropriate conditions.

Throughout this work, we considered an effective 1D model and used the single-active-electron approximation. Solving the time-dependent Schrödinger equation under these two approximations captures all the essential features of traditional HHG. In particular, 1D simulations are well-suited for qualitative study of spectrum for simple single-electron potentials. 1D approximation is inaccurate for complex molecules with significant electron motion in multiple dimensions or nonzero angular momentum as well as for elliptically polarized driving field. The single-active electron approximation on the other hand is most appropriate for atoms with low number of valence electrons and solid-state systems. For atoms with multiple electrons and complex molecules, additional effects will have to be considered.

The interharmonic spectral lines are a basic form of a broader phenomenon, foretelling an ample variety of interharmonic spectra, which can be achieved by considering systems with a larger number of isolated bound states. In particular, one may consider increasing the number of wells to infinite, reaching the regime of solid-state HHG and extending the isolated bound states to energy bands.

The interharmonic phenomena that we described here are universal to a wide range of systems, and can be described by different theoretical approaches, with the same qualitative features we predicted. For example, a complementary approach to describe interharmonic generation could rely on an internal self-phase modulation, as discussed in the Supporting Information, following refs 4−6. We believe that HIG tunable via adjustment of the driving field is a valuable tool in attosecond science, spectroscopy, promising tunability of X-ray sources, quantum coherent control of core electrons, and generation of attosecond pulses with desired properties.

https://doi.org/10.1021/acsphotonics.4c02095
ACS Photonics XXXX, XXX, XXX−XXX

METHODS

Throughout this work, we employ a 1D model in which an electron is bound to a stationary potential and driven by an external, linearly polarized, classical field. Ionization is introduced by considering finite potential wells with free particle propagation outside of the potential. The time-dependent Schrödinger equation (TDSE) is integrated via the Crank−Nicolson method.[53] In addition, to avoid reflections from the boundaries, the wave function is multiplied by a mask function which decays as $\cos^{1/8}(x), x \in [0,\pi/2]$ at the boundaries.[54] This mechanism also introduces a decrease in the wave function's normalization, effectively modeling the depletion of the driven atom. Unless mentioned explicitly, the normalization of the wave function is kept above 0.8 for all the simulations. All the parameters of the simulation can be found in Tables S1−S3 in the Supporting Information.

The high-harmonic generation (HHG) spectrum is evaluated within the single-active electron approximation.[55] The atomic part of the Hamiltonian is given by

$$H_a(x) = \frac{\hbar^2}{2m}\frac{d^2}{dx^2} + \mathcal{V}_a(x) \tag{4}$$

where m is the mass of the electron and $\mathcal{V}_a(x)$ is the stationary potential to which it is confined. The eigenenergies of the isolated bound states (the two eigenenergies contributing to the noninteger harmonics) are denoted by ε_g and ε_e, and the corresponding energy separation is given, in frequency units, by $\hbar\omega_a = |\varepsilon_e - \varepsilon_g|$.

The external driving field is introduced by adding the following interaction term to the Hamiltonian

$$H_I(x, t) = -exE(t) \tag{5}$$

where $E(t) = p(t)E\sin(\omega_d t)$, $p(t)$ is the pulse envelope, E is the maximal amplitude of the pulse, and ω_d is the driving frequency. The Rabi frequency, Ω_R, proportional to E, is defined as $\langle g|ex E|e\rangle$. In this work, we determine it by fitting the interharmonic spectral lines to those of the ideal TLS (see Supporting Information).

We consider both a Gaussian envelope, given by

$$p(t) = \exp\left[-\frac{4\log 2}{\tau_{FWHM}^2}\left(t - \frac{\tau_{FWHM}}{2}\right)^2\right] \tag{6}$$

where τ_{fwhm} is the fwhm duration, and a trapezoidal envelope, given by

$$p(t) = \begin{cases} \frac{t}{\tau_{on}}, & 0 < t < t_{on} \\ 1, & t_{on} < t < \tau - \tau_{off} \\ -\frac{t-\tau}{\tau_{off}}, & \tau - \tau_{off} < t < \tau \end{cases} \tag{7}$$

where τ is the duration of the entire pulse and τ_{on} (τ_{off}) is the turn on (off) period of the pulse. The above durations are defined by the number of periods of the driving field, $\sin(\omega_d t)$, occupying each duration. Therefore, a trapezoidal pulse envelope is fully characterized by the tuple (n_{on}, n_p, n_{off}), where n_I is the number of periods in the corresponding duration. Similarly, the pulse envelope of a Gaussian pulse is determined by n_{fwhm}. The relation between I and τ_I is given by $\tau_i = 2\pi n_i/\omega_d$.

The total time-dependent Hamiltonian reads

$$H(x, t) = H_a(x) + H_I(x, t) \tag{8}$$

Employing the dipole acceleration, which is given by

$$\ddot{d}(t) = \frac{d^2\langle ex\rangle}{dt^2} = -\langle e\Psi(x, t)|[H(x, t), [H(x, t), x]]|\Psi(x, t)\rangle \tag{9}$$

the emission spectrum is proportional to[56,57]

$$\mathcal{D}(\omega) = \left|\frac{1}{\omega^2}\int_{-\infty}^{\infty} dt\ddot{d}(t)e^{-i\omega t}\right|^2 \tag{10}$$

The stationary potentials employed in the previous sections, $V_a(x)$, are comprised of combinations of single soft-Coulomb potential wells, separated from each other by distance d. Each such well is given by

$$\mathcal{V}_{s.c.}(x) = \frac{1}{\sqrt{ax^2 + b}} \tag{11}$$

where a and b, along with d, are parameters that determine the bound states of the entire stationary Hamiltonian.

Controlling the number of potential wells and the values of a and b affects the eigenenergies of the isolated bound states and allows for fine-tuning the interharmonic spectral lines of the emitted radiation.

ASSOCIATED CONTENT

Supporting Information

The Supporting Information is available free of charge at https://pubs.acs.org/doi/10.1021/acsphotonics.4c02095.

Additional information on the calculation of physical quantities, comparison to ideal two-level systems and all the parameters used in the simulations (PDF)

AUTHOR INFORMATION

Corresponding Author

Ido Kaminer − *Technion − Israel Institute of Technology, Haifa 3200003, Israel;* orcid.org/0000-0003-2691-1892; Email: kaminer@technion.ac.il

Authors

Sergey Hazanov − *Technion − Israel Institute of Technology, Haifa 3200003, Israel; Weizmann Institute of Science, Rehovot 7610001, Israel*

Alexey Gorlach − *Technion − Israel Institute of Technology, Haifa 3200003, Israel*

Ron Ruimy − *Technion − Israel Institute of Technology, Haifa 3200003, Israel*

Dmitry Yakushevskiy − *Technion − Israel Institute of Technology, Haifa 3200003, Israel*

Matan Even Tzur − *Technion − Israel Institute of Technology, Haifa 3200003, Israel*

Marcelo F. Ciappina − *Technion − Israel Institute of Technology, Haifa 3200003, Israel; Department of Physics and Guangdong Provincial Key Laboratory of Materials and Technologies for Energy Conversion, Guangdong Technion - Israel Institute of Technology, Shantou, Guangdong 515063, China;* orcid.org/0000-0002-1123-6460

Complete contact information is available at: https://pubs.acs.org/10.1021/acsphotonics.4c02095

Author Contributions

#These authors contributed equally to this work (S.H. and A.G.).

Funding

This research is partially supported under the Flagship research project QUBIT by the Helen Diller Quantum Center at the Technion and the Israel Science Foundation (ISF), Grant No. 385/23. A.G. gratefully acknowledges Azrieli Scholarship. M.F.C. acknowledges support by the National Key Research and Development Program of China (Grant No. 2023YFA1407100), Guangdong Province Science and Technology Major Project (Future functional materials under extreme conditions -2021B0301030005), and the Guangdong Natural Science Foundation (General Program Project No. 2023A1515010871).

Notes

The authors declare no competing financial interest.

REFERENCES

(1) McPherson, A.; Gibson, G.; Jara, H.; Johann, U.; Luk, T. S.; McIntyre, I. A.; Boyer, K.; Rhodes, C. K. Studies of multiphoton production of vacuum-ultraviolet radiation in the rare gases. *J. Opt. Soc. Am. B* **1987**, *4*, 595−601.

(2) Corkum, P. B. Plasma perspective on strong field multiphoton ionization. *Phys. Rev. Lett.* **1993**, *71*, 1994−1997.

(3) Lewenstein, M.; Balcou, Ph.; Ivanov, M. Yu.; L'Huillier, A.; Corkum, P. B. Theory of high-harmonic generation by low-frequency laser fields. *Phys. Rev. A* **1994**, *49*, 2117−2132.

(4) Alfano, R. R.; Shapiro, S. L. Direct Distortion of Electronic Clouds of Rare-Gas Atoms in Intense Electric Fields. *Phys. Rev. Lett.* **1970**, *24*, 1217−1220.

(5) Alfano, R. R.; Mazhar, S. F. B.; Shi, L. Higher harmonic and supercontinuum generation arising from electronic self-phase modulation under ultrafast laser pulses for various states of matter. *Optik* **2021**, *247*, 167872.

(6) Alfano, R. R.; Mazhar, S. F. B. Higher harmonics and supercontinuum generated from the Kerr response time in different states of matter from a universal electromagnetic model. *Sci. Rep.* **2023**, *13*, 15467.

(7) Kreibich, T.; Lein, M.; Engel, V.; Gross, E. K. U. Even-Harmonic Generation due to Beyond-Born-Oppenheimer Dynamics. *Phys. Rev. Lett.* **2001**, *87*, 103901.

(8) Silva, R. E. F.; Rivière, P.; Morales, F.; Smirnova, O.; Ivanov, M.; Martín, F. Even harmonic generation in isotropic media of dissociating homonuclear molecules. *Sci. Rep.* **2016**, *6*, 32653.

(9) Neufeld, O.; Ayuso, D.; Decleva, P.; Ivanov, M. Y.; Smirnova, O.; Cohen, O. Ultrasensitive Chiral Spectroscopy by Dynamical Symmetry Breaking in High Harmonic Generation. *Phys. Rev. X* **2019**, *9*, 031002.

(10) Tzur, M. E.; Neufeld, O.; Fleischer, A.; Cohen, O. Selection rules for breaking selection rules. *New J. Phys.* **2021**, *23*, 103039.

(11) Neufeld, O.; Podolsky, D.; Cohen, O. Floquet group theory and its application to selection rules in harmonic generation. *Nat. Commun.* **2019**, *10*, 405.

(12) Liu, H.; Li, Y.; You, Y. S.; Ghimire, S.; Heinz, T. F.; Reis, D. A. High-harmonic generation from an atomically thin semiconductor. *Nat. Phys.* **2017**, *13*, 262−265.

(13) Vaswani, C.; Mootz, M.; Sundahl, C.; Mudiyanselage, D. H.; Kang, J. H.; Yang, X.; Cheng, D.; Huang, C.; Kim, R. H. J.; Liu, Z.; Luo, L.; Perakis, I. E.; Eom, C. B.; Wang, J. Terahertz Second-Harmonic Generation from Lightwave Acceleration of Symmetry-Breaking Nonlinear Supercurrents. *Phys. Rev. Lett.* **2020**, *124*, 207003.

(14) Schmid, C. P.; Weigl, L.; Grössing, P.; Junk, V.; Gorini, C.; Schlauderer, S.; Ito, S.; Meierhofer, M.; Hofmann, N.; Afanasiev, D.; Crewse, J.; Kokh, K. A.; Tereshchenko, O. E.; Güdde, J.; Evers, F.; Wilhelm, J.; Richter, K.; Höfer, U.; Huber, R. Tunable non-integer high-harmonic generation in a topological insulator. *Nature* **2021**, *593*, 385−390.

(15) Millack, T.; Maquet, A. Hyper-Raman Lines Produced During High Harmonic Generation. *J. Mod. Opt.* **1993**, *40*, 2161−2171.

(16) Bloch, E.; Beaulieu, S.; Descamps, D.; Petit, S.; Légaré, F.; Magunov, A.; Mairesse, Y.; Strelkov, V. Hyper-Raman lines emission concomitant with high-order harmonic generation. *New J. Phys.* **2019**, *21*, 073006.

(17) Hamer, K. A.; Mauger, F.; Folorunso, A. S.; Lopata, K.; Jones, R. R.; DiMauro, L. F.; Schafer, K. J.; Gaarde, M. B. Characterizing particle-like charge-migration dynamics with high-order harmonic sideband spectroscopy. *Phys. Rev. A* **2022**, *106*, 013103.

(18) Tritschler, T.; Mücke, O. D.; Wegener, M. Extreme nonlinear optics of two-level systems. *Phys. Rev. A* **2003**, *68*, 033404.

(19) Mollow, B. R. Power Spectrum of Light Scattered by Two-Level Systems. *Phys. Rev.* **1969**, *188*, 1969−1975.

(20) Hughes, S. Breakdown of the Area Theorem: Carrier-Wave Rabi Flopping of Femtosecond Optical Pulses. *Phys. Rev. Lett.* **1998**, *81*, 3363−3366.

(21) Plaja, L.; Roso-Franco, L. Adiabatic theory for high-order harmonic generation in a two-level atom. *J. Opt. Soc. Am. B* **1992**, *9*, 2210−2213.

(22) Kaplan, A. E.; Shkolnikov, P. L. Superdressed two-level atom: Very high harmonic generation and multiresonances. *Phys. Rev. A* **1994**, *49*, 1275−1280.

(23) Gauthey, F. I.; Garraway, B. M.; Knight, P. L. High harmonic generation and periodic level crossings. *Phys. Rev. A* **1997**, *56*, 3093−3096.

(24) Figueira de Morisson Faria, C.; Rotter, I. High-order harmonic generation in a driven two-level atom: Periodic level crossings and three-step processes. *Phys. Rev. A* **2002**, *66*, 013402.

(25) Bavli, R.; Metiu, H. Properties of an electron in a quantum double well driven by a strong laser: Localization, low-frequency, and even-harmonic generation. *Phys. Rev. A* **1993**, *47*, 3299−3310.

(26) Dakhnovskii, Y.; Bavli, R. Selective manipulation of the emission spectrum of an electron in a biased double-well heterostructure driven by a free-electron laser. *Phys. Rev. B* **1993**, *48*, 11010−11013.

(27) Zuo, T.; Chelkowski, S.; Bandrauk, A. D. Harmonic generation by the H2+ molecular ion in intense laser fields. *Phys. Rev. A* **1993**, *48*, 3837−3844.

(28) Ciappina, M. F.; Pérez-Hernández, J. A.; Landsman, A. S.; Zimmermann, T.; Lewenstein, M.; Roso, L.; Krausz, F. Carrier-Wave Rabi-Flopping Signatures in High-Order Harmonic Generation for Alkali Atoms. *Phys. Rev. Lett.* **2015**, *114*, 143902.

(29) Gaal, P.; Kuehn, W.; Reimann, K.; Woerner, M.; Elsaesser, T.; Hey, R.; Lee, J. S.; Schade, U. Carrier-wave Rabi flopping on radiatively coupled shallow donor transitions in n-type GaAs. *Phys. Rev. B* **2008**, *77*, 235204.

(30) Golde, D.; Meier, T.; Koch, S. W. High harmonics generated in semiconductor nanostructures by the coupled dynamics of optical inter- and intraband excitations. *Phys. Rev. B* **2008**, *77*, 075330.

(31) Wang, G.; Liu, Y.-X.; Cappellaro, P. Observation of the high-order Mollow triplet by quantum mode control with concatenated continuous driving. *Phys. Rev. A* **2021**, *103*, 022415.

(32) Wang, G.; Li, C.; Cappellaro, P. Observation of Symmetry-Protected Selection Rules in Periodically Driven Quantum Systems. *Phys. Rev. Lett.* **2021**, *127*, 140604.

(33) Ghimire, S.; Reis, D. A. High-harmonic generation from solids. *Nat. Phys.* **2019**, *15*, 10−16.

(34) Ghimire, S.; DiChiara, A. D.; Sistrunk, E.; Agostini, P.; DiMauro, L. F.; Reis, D. A. Observation of high-order harmonic generation in a bulk crystal. *Nat. Phys.* **2011**, *7*, 138−141.

(35) Heide, C.; Kobayashi, Y.; Haque, S. R. U.; Ghimire, S. Ultrafast high-harmonic spectroscopy of solids. *Nat. Phys.* **2024**, *20*, 1546−1557.

(36) Schubert, O.; Hohenleutner, M.; Langer, F.; Urbanek, B.; Lange, C.; Huttner, U.; Golde, D.; Meier, T.; Kira, M.; Koch, S. W.; Huber, R. Sub-cycle control of terahertz high-harmonic generation by dynamical Bloch oscillations. *Nat. Photonics* **2014**, *8*, 119−123.

(37) Scully, M. O.; Zubairy, M. S. *Quantum Optics*; Cambridge University Press, 1997.

https://doi.org/10.1021/acsphotonics.4c02095
ACS Photonics XXXX, XXX, XXX−XXX

(38) Wegner, M. *Extreme Nonlinear Optics*; Springer-Verlag: Berlin/Heidelberg, 2005.
(39) Gomez Llorente, J. M.; Plata, J. Tunneling control in a two-level system. *Phys. Rev. A* **1992**, *45*, R6958−R6961.
(40) Grossmann, F.; Dittrich, T.; Jung, P.; Hänggi, P. Coherent destruction of tunneling. *Phys. Rev. Lett.* **1991**, *67*, 516−519.
(41) Joannopoulos, J. D.; Johnson, S. G.; Winn, J. N.; Meade, R. D. *Photonic crystals: molding the flow of light*; Princeton University Press, 2008.
(42) Itatani, J.; Levesque, J.; Zeidler, D.; Niikura, H.; Pépin, H.; Kieffer, J. C.; Corkum, P. B.; Villeneuve, D. M. Tomographic imaging of molecular orbitals. *Nature* **2004**, *432*, 867−871.
(43) Mücke, O. D.; Tritschler, T.; Wegener, M.; Morgner, U.; Kärtner, F. X. Signatures of Carrier-Wave Rabi Flopping in GaAs. *Phys. Rev. Lett.* **2001**, *87*, 057401.
(44) Sivis, M.; Taucer, M.; Vampa, G.; Johnston, K.; Staudte, A.; Naumov, A. Yu.; Villeneuve, D. M.; Ropers, C.; Corkum, P. B. Tailored semiconductors for high-harmonic optoelectronics. *Science* **2017**, *357*, 303−306.
(45) Lukashov, S.; Petrov, A.; Pravilov, A. *The Iodine Molecule*; Springer International Publishing, 2018.
(46) Hay, N.; Velotta, R.; Mason, M. B.; Castillejo, M.; Marangos, J. P. High-order harmonic generation efficiency increased by controlled dissociation of molecular iodine. *J. Phys. B: At. Mol. Opt. Phys.* **2002**, *35*, 1051.
(47) Clarke, J. Flux Qubit Completes the Hat Trick. *Science* **2003**, *299*, 1850−1851.
(48) Baur, M.; Filipp, S.; Bianchetti, R.; Fink, J. M.; Göppl, M.; Steffen, L.; Leek, P. J.; Blais, A.; Wallraff, A. Measurement of Autler-Townes and Mollow Transitions in a Strongly Driven Superconducting Qubit. *Phys. Rev. Lett.* **2009**, *102*, 243602.
(49) Shillito, R.; Petrescu, A.; Cohen, J.; Beall, J.; Hauru, M.; Ganahl, M.; Lewis, A. G. M.; Vidal, G.; Blais, A. Dynamics of Transmon Ionization. *Phys. Rev. Appl.* **2022**, *18*, 034031.
(50) Nojiri, Y.; Honasoge, K. E.; Marx, A.; Fedorov, K. G.; Gross, R. Onset of transmon ionization in microwave single-photon detection. *Phys. Rev. B* **2024**, *109*, 174312.
(51) Kayanuma, Y.; Saito, K. Coherent destruction of tunneling, dynamic localization, and the Landau-Zener formula. *Phys. Rev. A* **2008**, *77*, 010101.
(52) Ghimire, S.; DiChiara, A. D.; Sistrunk, E.; Ndabashimiye, G.; Szafruga, U. B.; Mohammad, A.; Agostini, P.; DiMauro, L. F.; Reis, D. A. Generation and propagation of high-order harmonics in crystals. *Phys. Rev. A* **2012**, *85*, 043836.
(53) Wells, D.; Quiney, H. A fast and adaptable method for high accuracy integration of the time-dependent Schrödinger equation. *Sci. Rep.* **2019**, *9*, 782.
(54) Krause, J. L.; Schafer, K. J.; Kulander, K. C. Calculation of photoemission from atoms subject to intense laser fields. *Phys. Rev. A* **1992**, *45*, 4998−5010.
(55) Joachain, C. J. Atoms in Intense Laser Fields. In *Supercomputing, Collision Processes, and Applications*; Bell, K. L., Berrington, K. A., Crothers, D. S. F., Hibbert, A., Taylor, K. T., Eds.; Springer, 1999; pp 77−103.
(56) Schafer, K. J.; Kulander, K. C. High Harmonic Generation from Ultrafast Pump Lasers. *Phys. Rev. Lett.* **1997**, *78*, 638−641.
(57) Ciappina, M. F.; Biegert, J.; Quidant, R.; Lewenstein, M. High-order-harmonic generation from inhomogeneous fields. *Phys. Rev. A* **2012**, *85*, 033828.

https://doi.org/10.1021/acsphotonics.4c02095
ACS Photonics XXXX, XXX, XXX−XXX